Melendez, A.J., Carlson, K.D., and Beckermann, C., "Simulation of Reoxidation Inclusion Formation in Steel Casting," in Proceedings of the 61st SFSA Technical and Operating Conference, Paper No. 3.8, Steel Founders' Society of America, Chicago, IL, 2007.

Simulation of Reoxidation Inclusion Formation in Steel Casting

Antonio J. Melendez, Kent D. Carlson and Christoph Beckermann

Department of Mechanical and Industrial Engineering

The University of Iowa, Iowa City, IA 52242

Abstract

A combined theoretical and experimental study is performed to investigate the formation of reoxidation inclusions in carbon and low-alloy steel castings. A model is developed that predicts the growth, agglomeration, and motion of oxide inclusions during pouring. The model is implemented in the casting simulation software MAGMAsoft. Measurements of total inclusion number density and volume fraction are conducted using radiographs of cast steel weld plates. The limit of resolution in the radiographs is about 1.5 mm (~1/16 in). The measurements show that the inclusion number density in the plates varies from zero to almost 70,000 m^{-3} (~2000 ft^{-3}), while the inclusion volume fraction reaches values as high as 1,700 ppm (~3 in^3/ft^3). These measurements are used to tune and validate the simulation model predictions. A characteristic free surface length of 4 mm (0.16 in) and an agglomeration length of 3 mm (0.12 in) in the model are found to yield predictions that approximately agree with the measurements. However, considerable uncertainty exists with respect to the presence of large inclusions in the plates, particularly below the risers, and the ability of inclusions to adhere to mold walls. Recommendations for future research on reoxidation inclusion formation are made.

1. Introduction

The removal of oxide inclusions from castings and the subsequent repair of those castings are expensive and time consuming procedures. Svoboda et al.[1] estimated that twenty percent of the cost of producing castings is due to the removal of inclusions and the repair of the resulting defect areas with weld metal. Inclusions that remain in the casting adversely affect machining and mechanical performance, and may cause the casting to be rejected for failing to meet the radiographic standard requirements specified by the customer regarding allowable inclusion severity. Reoxidation inclusions, which form when deoxidized steel comes into contact with oxygen during mold filling, make up a substantial portion of the inclusions found in steel castings. Griffin and Bates[2] estimated that 83% of the macro-inclusions found in low-alloy steel castings are reoxidation inclusions, as are 48% of those found in high-alloy steel castings. The primary source of oxygen in reoxidation inclusion formation is air, which contacts the metal stream during pouring and the metal free surface in the mold cavity during filling.

At present, trial-and-error and experience are the only tools that foundry engineers have at their disposal to solve inclusion problems in steel castings. If a casting has inclusion problems, the foundry engineer may change the pouring practice or gating design for the casting in hopes that this will eliminate or reduce the severity of the problem. Changing the pouring or gating will change melt flow patterns during filling. This may reduce the amount of reoxidation inclusions created, or it may merely change the final location of macro-inclusions; if the inclusions are swept into a riser rather than collecting on the cope surface of the casting, the inclusion problem is solved even if the volume of reoxidation inclusions created does not change. In order to avoid inclusion problems or to reduce their severity, foundries often employ special gating techniques to reduce the contact area and time between the melt and the atmosphere during mold filling or to trap inclusions inside the runners. However, while a poor gating system can create inclusion problems in castings, a good gating system will not necessarily prevent inclusion problems. Thus, several iterations on the rigging of a casting may be necessary to resolve inclusion issues.

In an attempt to provide foundry engineers with a tool for eliminating or minimizing inclusion problems, a model is being developed that simulates the formation, growth, and motion of reoxidation inclusions during the pouring of carbon and low-alloy steel castings. This model, which is being developed within the commercial casting simulation software MAGMAsoft[3], will allow foundries to predict the final location, size, number and other characteristics of reoxidation inclusions in a casting. This information can be used to help determine whether or not a given mold design will lead to inclusion problems, without having to expend the time, effort and money to produce the casting to determine this information.

The objective of this study is to perform a preliminary experimental validation of the present version of the inclusion simulation model. The various components of the inclusion model that are currently implemented in MAGMAsoft are described in Section 2. The experiments are detailed in Section 3, and the measured and predicted results are compared in Section 4. The conclusions and recommendations for future research are summarized in Section 5.

2. Modeling Reoxidation Inclusions

The inclusion calculations described in this section are performed as part of a standard filling simulation in MAGMAsoft. In a standard filling simulation, the melt velocities and free surface geometry are calculated as a function of time during mold filling. The present model also tracks inclusions, in a Lagrangian sense. The model assumes that the reoxidation inclusions are spherical, characterized by their diameter, d_{inc} (cm), as depicted in figure 1. The oxide mixture that forms during the pouring of carbon and low-alloy steel is partially liquid[4], as opposed to the solid oxide films or particles that form during casting of high-alloy steel or light metals, and can thus be approximated as droplets. The inclusions form and grow on the melt free surface, and they are transported through the mold cavity by melt flow. Additionally, inclusions can combine (agglomerate). This section describes the models for inclusion birth, growth, agglomeration and motion. Additional detail regarding these models can be found in references [4] and [5].

Birth

The birth mechanism creates tiny new inclusions on the free surface of the melt during filling. The mechanism functions by searching the melt free surface for inclusions. In regions of the free surface already containing at least one inclusion, no inclusions are added. However, if a region of the free surface does not contain any inclusions, then inclusions are added to this region with a user-specified spacing of L_{birth} (cm). This is depicted in figure 2. The initial size of the inclusions that nucleate on the free surface, d_{birth} (cm), is assumed to be negligibly small. In practice, a small but finite value for the birth diameter is used, such that the initial inclusion volume is still negligibly small. The primary purpose of the birth mechanism is to ensure that there are inclusions throughout the entire free surface of the melt. This is important in order to obtain the correct amount of oxide on the free surface; as described in the next sub-section, oxide produced by melt-air interaction is apportioned to inclusions, causing them to grow. If no inclusions are present on a region of the free surface, the oxide that should form in that region would be lost.

Growth

The growth of reoxidation inclusions is assumed to be controlled by the mass transfer of oxygen through the air to the melt-air interface. A detailed discussion of this assumption can be found in reference [4]. When an inclusion is on the melt free surface, it grows according to the following mass balance equation:

$$\frac{\partial V_{inc}}{\partial t} = A_{FS,inc}\beta \tag{1}$$

In equation (1), V_{inc} is the inclusion volume (cm^3); t is time (s); β is the overall mass transfer coefficient (cm/s); and $A_{FS,inc}$ represents the area (cm^2) of the melt free surface that is contributing oxide to the growing inclusion. This area is determined by dividing the total free surface area of a computational cell in which the inclusion currently resides among all of the inclusions within that flow cell, proportional to each inclusion's surface area. This is depicted in figure 3. Equation (1) shows that inclusion growth is directly proportional to both the mass transfer coefficient and area of the melt free surface that is contributing oxide to the growing

inclusion. Note that this equation also implies that only inclusions on the free surface will grow, since $A_{FS,inc} = 0$ away from the free surface; this is physically realistic, because the oxygen required for significant reoxidation inclusion growth is not available away from the melt free surface.

The growth rate of reoxidation inclusions via the model described in equation (1) is controlled by the overall mass transfer coefficient, β, which can be expressed as[4]:

$$\beta = \frac{r_{inc} M_{inc}}{\rho_{inc}} \frac{D_{O_2}}{\delta_{O_2}} \frac{p_{O_2}}{\overline{R} T} \tag{2}$$

where r_{inc} is the ratio of the number of moles of inclusions to the number of moles of diatomic oxygen (O_2) consumed; M_{inc} is the effective molecular weight of the inclusions (g/mol); ρ_{inc} is the effective inclusion density (g/cm^3); D_{O_2} is the mass diffusivity of O_2 gas in the atmosphere (cm^2/s); p_{O_2} is the partial pressure of O_2 gas in the atmosphere (Pa); T is the air temperature (K) at the melt-air interface; $\overline{R}$ is the universal gas constant; and δ_{O_2} is the thickness of the oxygen boundary layer (cm) at the melt free surface (see figure 4). Values for the various properties and constants used in the present calculations are listed in table 1. The carbon monoxide gas that forms during oxidation of carbon and low-alloy steels during pouring is not taken into account[4]. It is seen from equation (2) that the mass transfer coefficient is proportional to the partial pressure of molecular oxygen, and is inversely proportional to the boundary layer thickness.

Table 1: Properties and Constants Used in the Inclusion Simulations [4]

Quantity	**Value**
Effective molecular weight of inclusions (M_{inc})	149 g/mol
Inclusion moles per mole of molecular oxygen (r_{inc})	0.42
Effective inclusion density (ρ_{inc})	3.23 g/cm^3
Birth diameter (d_{birth})	10 μm (0.001 cm)
Kinematic viscosity of air (ν_a)	3.53 cm^2/s
Diffusivity of oxygen in air (D_{O_2})	4.56 cm^2/s
Partial pressure of oxygen in air (p_{O_2})	21287.25 Pa
Density of liquid steel (ρ_l)	6.95 g/cm^3
Kinematic viscosity of liquid steel (ν_l)	0.00648 cm^2/s
Universal gas constant $(\overline{R})$	8.314×10^6 Pa·cm^3/(mol·K)
Gravitational acceleration (g)	981 cm/s^2

The oxygen boundary layer thickness, δ_{O_2}, is a function of the relative velocity between the melt free surface and the air, a characteristic length of the melt free surface, and various air properties. The boundary layer thickness can be determined through consideration of a

dimensionless parameter known as the Sherwood number, Sh, which is defined as the ratio of the melt free surface characteristic length, L_c (cm), to the boundary layer thickness, δ_{O_2} :

$$\mathrm{Sh} = \frac{L_c}{\delta_{O_2}} = 2 + 0.6\,\mathrm{Re}^{1/2}\,\mathrm{Sc}^{1/3} \tag{3}$$

The second equality in equation (3) indicates that the Ranz-Marshall correlation[6] is used to estimate the Sherwood number as a function of the Reynolds and Schmidt numbers. The Reynolds number is defined as $\mathrm{Re} = u_s L_c / \nu_a$, where ν_a is the kinematic viscosity of the air (cm^2/s), and u_s is the magnitude of the relative velocity (cm/s) between the melt free surface and the air. Assuming that the air velocity is negligible, u_s is approximated as the magnitude of the melt velocity at the free surface. The Schmidt number is defined as $\mathrm{Sc} = \nu_a / D_{O_2}$. Values for the various properties are provided in table 1.

The variation of the boundary layer thickness with the characteristic length and relative velocity, according to equation (3), is plotted in figure 5. The boundary layer thickness decreases as the relative velocity increases, and increases as the characteristic length increases. The local characteristic length of the melt free surface during pouring is generally unknown. If the liquid metal stream were to consist of droplets, L_c would be equal to the droplet diameter. For other metal stream geometries, the Ranz-Marshall correlation can still be used to obtain a first estimate of the boundary layer thickness and the characteristic length should then be interpreted as an effective diameter or length of a portion of the free surface. For sufficiently large melt velocities, such as those typical in steel casting (e.g., $u_s > 100$ cm/s), the dependence of the boundary layer thickness on the characteristic length is not very strong ($\delta_{O_2} \sim L_c^{1/2}$); this can also be seen in figure 5. Therefore, as a very first approximation in the present model, the characteristic length is assumed to be a constant that is the same at every point on the free surface and does not vary with time. A suitable effective value for the characteristic length is determined in the next section through a comparison of measured and predicted inclusion volume fractions and number densities in a steel casting. At present, only approximate bounds can be estimated for the characteristic length in pouring of steel castings: (*i*) lower bound: ~ 1 to 2 mm, being the diameter of the smallest steel droplets that may form during pouring; (*ii*) upper bound: ~ 10 to 20 mm, being the diameter of the largest liquid steel jet before breakup occurs. It is anticipated that a future version of the inclusion model may incorporate an equation for calculating the local characteristic length from the knowledge of the instantaneous free surface geometry (as provided by a filling simulation). However, to develop such an equation, carefully designed experiments under a wide range of conditions must be performed in order to obtain the data necessary for calibration.

Equations (1) to (3) fully describe the growth rate of a single inclusion at the melt free surface. The increase in volume is calculated (at each time step) as a function of the surface area apportioned to each inclusion, the local melt surface velocity and the characteristic free surface length. To better understand the effects of the melt velocity and characteristic length, it is useful to use the present growth model to estimate the total reoxidation inclusion volume that forms during pouring of a steel casting. Summing over all inclusions and assuming, for this estimate

only, that the mass transfer coefficient β is constant with time and the same for all inclusions, equation (1) can be integrated over the pour time to yield:

$$V_{inc,total} = \beta \int_0^{t_{pour}} A_{FS}\, dt = \beta \overline{A}_{FS} t_{pour} \tag{4}$$

where $V_{inc,total}$ (cm^3) is the volume of all inclusions formed during the pour time, t_{pour}, of the casting, and A_{FS} (cm^2) is the total free surface area at time t. The second equality in equation (4) uses the mean value theorem to define a mean free surface area, $\overline{A}_{FS}$ (cm^2). The area-time integral, $\int_0^{t_{pour}} A_{FS}\, dt$, can readily be obtained from a filling simulation. The inclusion volume fraction in the casting, f_{inc}, is then given by

$$f_{inc} = \frac{V_{inc,total}}{V_s} = \beta \frac{\overline{A}_{FS} t_{pour}}{V_s} \tag{5}$$

where V_s (cm^3) is the total volume of steel that is poured. To find the total inclusion volume fraction, β is calculated from equations (2) and (3) as a function of L_c and u_s. In order to obtain a representative value for the ratio $\overline{A}_{FS} t_{pour} / V_s$ in equation (5), a filling simulation was performed of the casting described in the next section; this simulation gave $\overline{A}_{FS} t_{pour} / V_s \approx 0.37$ s/cm. The inclusion volume fraction obtained in this manner is plotted in figure 6 against the characteristic length, with the melt velocity as a parameter. The inclusion volume fraction is shown in parts per million (ppm) on the left vertical axis, and in cubic inches of inclusions per cubic foot of steel on the right vertical axis. The total inclusion volume fraction increases as the characteristic length decreases; this effect is minor for characteristic lengths above 5 to 10 mm (particularly for small melt velocities), but becomes very pronounced as the characteristic length decreases below 5 mm. As expected, the inclusion volume fraction also increases with increasing melt velocity; again, this effect is relatively minor for large characteristic lengths, but quite strong for characteristic lengths below about 5 mm. Thus, aside from the melt velocity and the free surface area, the inclusion volume fraction is strongly dependent on the characteristic length, L_c. A typical value[7] for the inclusion volume fraction in a steel casting is given by 1 in^3/ft^3 (~ 600 ppm). It can be seen from figure 6 that such an inclusion volume fraction is obtained by the present model (and melt velocities between 0 and 600 cm/s) if the characteristic length is between 2 and 6 mm. This range of characteristic lengths is realistic, given the geometry and pouring conditions of the casting under consideration (see below).

Agglomeration

As filling proceeds, inclusions can collide and coalesce, forming a single larger inclusion. This interaction, known as agglomeration, is considered in the present inclusion model. Agglomeration is controlled through the user specification of the agglomeration length, L_{agg} (cm). The agglomeration mechanism considers each inclusion, and finds all other inclusions

whose centers are within the distance L_{agg} from the center of the inclusion under consideration. All such inclusions within this distance are combined into a single, agglomerated inclusion, as shown schematically in figure 6. The mass of this new agglomerated inclusion is simply the sum of the mass of all the inclusions that were involved in the agglomeration. The agglomerated inclusion is placed at the center of mass of all the inclusions that were combined, and assigned a velocity that is determined through conservation of linear momentum among all of the agglomerated inclusions.

In the present implementation of the inclusion model, the two user-specified lengths for birth and agglomeration are set equal to each other (i.e., $L_{birth} = L_{agg}$). Specifying the birth length to be smaller than the agglomeration length would be meaningless, because new inclusions on the free surface would agglomerate together in the same time step in which they were created. The birth length could be made larger than the agglomeration length, but as the birth length is rather arbitrary, it is simpler to just use the same value for both lengths.

As with the melt free surface characteristic length, L_c, the agglomeration length, L_{agg}, is considered an adjustable constant in this study. The effect that the agglomeration length has on the simulated inclusions is investigated in the parametric studies below and a suitable value is determined through comparisons with experimental measurements. It is important to note that L_{agg} has no effect on the total amount of inclusions (or total inclusion volume fraction, f_{inc}) formed; this quantity is controlled by L_c, as explained in the previous subsection. However, the agglomeration length, L_{agg}, does control the number of inclusions (or number density, n_{inc}) formed, and therefore their size. In future versions of the model, the agglomeration length could be made a function of the local size, volume fraction and velocity of the inclusions.

Motion

In order to determine the final location of each inclusion in the casting, the motion of each inclusion is tracked from its birth until the end of filling. This is accomplished by solving the following equation of motion, for each inclusion at each time step:

$$\rho_{inc}\frac{d\boldsymbol{u}_{\boldsymbol{inc}}}{dt} = \underbrace{\frac{18\mu_l}{d_{inc}^2}\left(\boldsymbol{u}_{\boldsymbol{l}} - \boldsymbol{u}_{\boldsymbol{inc}}\right)\left(1 + 0.15\,\mathrm{Re}_{inc}^{0.687}\right)}_{\text{drag}} + \underbrace{\left(\rho_{inc} - \rho_l\right)\boldsymbol{g}}_{\text{bouyancy}} \tag{6}$$

In equation (6), Re_{inc} is the inclusion Reynolds number, $\mathrm{Re}_{inc} = \left|\boldsymbol{u}_{\boldsymbol{l}} - \boldsymbol{u}_{\boldsymbol{inc}}\right|\rho_l d_{inc}/\mu_l$, which is defined in terms of the magnitude of the relative velocity between the melt and the inclusion, $\left|\boldsymbol{u}_{\boldsymbol{l}} - \boldsymbol{u}_{\boldsymbol{inc}}\right|$ (cm). The melt velocity, $\boldsymbol{u}_{\boldsymbol{l}}$, available from the filling simulation, is interpolated to the location of the inclusion. The other parameters introduced in equation (6) are the density of the melt, ρ_l (g/cm^3); the dynamic viscosity of the melt, μ_l (g/cm-s); the density of the inclusion, ρ_{inc} (g/cm^3); and the gravity vector, $\boldsymbol{g}$ (cm/s^2).

During each time step of the filling simulation, equation (6) is solved for each inclusion to determine its velocity. This information is then used to update the location of each inclusion

according to $d\boldsymbol{x}_{inc}/dt = \boldsymbol{u}_{inc}$, where $\boldsymbol{x}_{inc}$ is the inclusion's position vector. If an inclusion comes into contact with a mold wall, there are two mutually exclusive approaches that have been adopted in this work. In the first approach, the inclusion sticks when it comes into contact with a mold wall. In the second approach, the inclusion is allowed to slip along the mold wall after contact. Both approaches are examined below.

3. Experiments

Measurements of the amount and size distribution of inclusions were made using radiographs for a total of 38 weld plates made of 1022 steel cast in a sand mold. A MAGMAsoft model of the steel casting is shown in figure 8. The plates had a length of 31.1 cm (12.25 in), a width of 18.7 cm (7.375 in) and a thickness of 3.2 cm (1.25 in). As shown in the figure, a weld groove and two large risers were present over some portions of the plate. The liquid steel was delivered into the mold from a bottom-pour ladle. The pouring temperature and time were, on the average, 1,581°C (2,878°F) and 5.5 s, respectively. The average liquid metal head height above the top of the pouring cup (see figure 8) was 46.7 cm (18.4 in). Prior to radiography, the risers and the gating system were removed from the plate.

A radiograph of one of the weld plates is shown in figure 9. The darker spots on this radiograph, up to several millimeters in diameter, are inclusions. Every visible inclusion was traced and counted. A superposition of the inclusion traces of the four "dirtiest" weld plates is shown in figure 10. It was not possible to trace inclusions at the location of the weld groove. It can be seen that the inclusions are uniformly distributed over the plate, except for approximately 5 cm (2 in) long by 2.5 cm (1 in) wide areas next to the two ingates. Presumably, the inclusions were swept away from these areas by the incoming metal streams. It is interesting to note that the inclusion density below the two risers appears to be approximately the same as in the remainder of the plate. Since inclusions are always lighter than the liquid steel, they may be expected to float up into the two risers, such that the areas below the risers are inclusion free. The presence of inclusions below the risers in the present experiments is somewhat surprising, but may be attributed to inclusions sticking to the drag surface of the mold.

In order to obtain quantitative data of the amount and size distribution of inclusions in the weld plates, the following very approximate procedure was adopted. Each (non-circular) inclusion trace was approximated as a circle of the same area as the actual trace. The diameter of the circle, d_{inc}, was measured and the volume of each inclusion was calculated from $V_{inc} = \pi d_{inc}^3/6$. It is noted that the inclusions are unlikely to be spherical in shape, but in the absence of additional information on their three-dimensional shape, the present method represents a reasonable first approximation. The total volume of all inclusions in each weld plate, $V_{inc,total}$, was then calculated by adding the volume of each inclusion over the total number of inclusions, N_{inc}, in a given weld plate. Finally, an inclusion volume fraction and number density were calculated for each weld plate, respectively, from

$$f_{inc} = \frac{V_{inc,total}}{V_s} \qquad \text{and} \qquad n_{inc} = \frac{N_{inc}}{V_s} \tag{7}$$

where V_s (cm^3) is the volume of steel in the plate (excluding the risers and gating). Since no inclusions could be detected at the location of the weld groove (see figure 9), the volume of steel obscured by the weld groove was subtracted from the total volume of the plate.

Figure 11 shows the measured inclusion number density (left graph) and volume fraction (right graph) for each of the 38 weld plates, ordered by increasing volume fraction. No inclusions were detected in 17 of the 38 weld plates. This does not imply that these "clean" plates are free of inclusions; they are simply devoid of inclusions that are detectable using the present radiographic procedure. Among the 21 "dirty" weld plates, large variations in the measured inclusion number density and volume fraction are observed in figure 11. The inclusion number density varies from zero to almost 70,000 m^{-3} (~2000 ft^{-3}), while the volume fraction reaches values as high as 1,700 ppm (~3 in^3/ft^3). Such large variations are not uncommon in steel casting, and the origin of such variations is largely unknown. Suffice it to say that the weld plates were cast from different heats and under a variety of conditions. For the 21 "dirty" weld plates, the measured average inclusion number density and volume fraction are 15,756 m^{-3} (446 ft^{-3}) and 239 ppm (0.41 in^3/ft^3), respectively.

The distributions provided in figure 12 show the measured inclusion number density (left graph) and volume fraction (right graph) as a function of the measured inclusion diameter, in 0.5 mm wide diameter bins. In these graphs, only the measurements for the 21 "dirty" weld plates are included. Since the number density and volume fraction are both on a 'per unit volume of steel' basis, the results in these graphs can be interpreted as averages over these 21 weld plates. It can be seen from figure 12 that the measured inclusion diameters range from 0.5 mm (~0.02 in) to 10 mm (~0.4 in), with the average being approximately 2.5 mm (0.1 in). The inclusion number density is the highest in the 1.5 to 2.0 mm diameter bin and decreases strongly as the largest diameter is approached. The inclusion number density also decreases for diameters below 1.5 mm (~1/16 in), but this is not a physical effect; the decrease is simply due to the difficulty in detecting inclusions with diameters below 1.5 mm (~1/16 in) on the radiographs. A reasonable value for the limit of resolution is 1.5 mm (~1/16 in), and all results below this diameter should be discarded. If all inclusions could be detected, the inclusion number density can be expected to rise up to at least 10^7 m^{-3} for inclusions with a diameter of the order of 10 μm[8]. Therefore, the average inclusion diameter is a strong function of the limit of resolution; if the smaller inclusions could be resolved, the average (mean) inclusion diameter would be much smaller. The right graph in figure 12 indicates that the limit of resolution plays a negligible role in the inclusion volume fraction distribution, because the inclusions that were detected with a diameter below 1.5 mm (~1/16 in) constitute only a very small portion of the total inclusion volume. The volume fraction distribution is relatively flat, since the relatively few large inclusions contribute significantly to the total inclusion volume.

Figure 12 provides the principle experimental results in a form suitable for comparison with simulation. For all inclusions larger than 1.5 mm (~1/16 in) in diameter, the average inclusion number density and volume fraction in the 21 "dirty" plates are 11,884 m^{-3} (~337 ft^{-3}) and 236 ppm (~0.4 in^3/ft^3), respectively. These measurements are used in the following section to tune and validate the model. In particular, having measurements of both the inclusion volume fraction and the number density should allow for the determination of both the characteristic free surface length, L_c, and the agglomeration length, L_{agg}. Recall that in the model, all inclusions

are assigned an initial diameter of 10 μm, and many of these small inclusions are swept away from the free surface and never increase in size. Due to the present limit of resolution in the measurements, it is important in the comparison between the experiments and the simulation to only "count" those inclusions in the predicted results that have grown or agglomerated to a diameter greater than 1.5 mm (~1/16 in).

4. Simulation of Experiments

The filling of the weld plate was simulated using a modified version of MAGMAsoft where the present inclusion model was implemented. The filling simulation parameters were chosen to correspond to the average pouring conditions described in the Experiments section. Figure 13 shows four snapshots of the filling simulation. The inclusions are visualized as small particles with a size proportional to the calculated inclusion diameter. The color scale also indicates the inclusion diameter. In this simulation, when inclusions come into contact with a mold wall, they are assumed to adhere to the wall. Also, the characteristic free surface length and the agglomeration length are chosen to be $L_c = 4$ mm and $L_{agg} = 3$ mm, respectively (see below). It can be seen that numerous small inclusions, close to their initial size, are predicted to exist throughout the volume of the melt during filling. A few larger inclusions can also be observed in various portions of the casting. A relatively high concentration of large inclusions, with diameters up to 6 mm, is present at the top of the two risers. Figure 14 shows an x-ray view of the predicted inclusions in the plate only (i.e., the two risers and the gating are removed from this picture). The larger inclusions present in the plate are all stuck to bounding mold walls.

Figure 15 shows the distributions of the inclusion number density (left graphs) and volume fraction (right graphs) predicted in this simulation. The upper two graphs provide the distributions for the entire casting, while the lower two graphs are for the plate only. The scales for the vertical axes in these graphs may seem inappropriate, but they were chosen to be identical to the ones used in figure 12 presenting the experimental results. It can be seen from figure 15 that, as expected, the predicted inclusion number density and volume fraction generally decrease with increasing inclusion diameter. The total inclusion number density and volume fraction (see insets) are somewhat higher in the plate than in the entire casting, implying that fewer reoxidation products are present in the risers and the gating. However, counting only the inclusions with a diameter greater than 1.5 mm, the volume fraction is somewhat higher in the entire casting than in the plate only. This is related to the fact that relatively few large inclusions are predicted to be present in the plate. In fact, the plate does not have any inclusions with a diameter greater than 2.5 mm (see figure 14). All larger inclusions (with diameters between 2.5 and 6 mm) are present at the top of the two risers (see figure 13). This can be attributed to the larger inclusions having a grater floatation speed than the small inclusions.

Figure 16 shows a comparison of the results of the current simulation (as presented in figure 13) with those of another simulation where the inclusions coming into contact with the mold wall are allowed to slide along the wall rather than sticking to it. In the latter case, no inclusions with a diameter greater than 0.5 mm are predicted to be present in the plate, as well as along the vertical walls of the risers and the gating/sprue. All larger inclusions, with diameters up to 7 mm, accumulate at the top of the two risers and the downsprue. Clearly, for larger inclusions to be present in the plate (and particularly below the two risers), it is necessary to assume in the model

that inclusions stick to the mold wall. Since the experiments revealed the presence of numerous large inclusions in the plate, the following simulations are all conducted with the assumption that inclusions stick to the mold walls.

The present values utilized for the characteristic free surface length and the agglomeration length (i.e., $L_c = 4$ mm and $L_{agg} = 3$ mm, respectively) were chosen based on the parametric study presented in figure 17. A total of 13 weld plate filling simulations were performed where L_c and L_{agg} were varied. The left graph in figure 17 shows the predicted inclusion number density as a function of L_{agg}, with L_c as a parameter, while the right graph shows the predicted inclusion volume fraction as a function of L_c, with L_{agg} as a parameter. In order to allow for a direct comparison with the experimental measurements, the predictions in figure 17 are for the plate only (i.e., not the entire casting). Furthermore, other than for the volume fraction curve labeled "all sizes", the number densities and volume fractions plotted in this figure are for inclusions with a diameter, d_{inc}, greater than 1.5 mm only. The corresponding measurements [11,884 m^{-3} (~337 ft^{-3}) and 236 ppm (~0.4 in^3/ft^3), respectively; see figure 12] are indicated in figure 17 as horizontal dashed lines. It can be seen from the right graph that, as expected from the discussion regarding figure 6, the inclusion volume fraction decreases with increasing L_c. For a given L_c, the number density and volume fraction of inclusions with $d_{inc} \geq 1.5$ mm increase strongly with increasing agglomeration length, L_{agg}. In other words, more large inclusions are formed as the agglomeration length is increased. The left graph in figure 17 shows that as the agglomeration length tends to zero, the number density of inclusions with $d_{inc} \geq 1.5$ mm vanishes, regardless of L_c. Hence, if agglomeration is not included in model ($L_{agg} = 0$) and the inclusions increase in size by growth only, the large ($d_{inc} \geq 1.5$ mm) reoxidation macro-inclusions observed in steel castings[1] cannot be predicted.

Based on the results in figure 17, it is difficult to choose characteristic and agglomeration lengths that result in simultaneous agreement with both the measured inclusion number density and the measured inclusion volume fraction. For L_c less than about 2 mm, the inclusion volume fraction corresponding to all inclusion sizes becomes unrealistically large [i.e., greater than ~1,000 ppm (~1.5 in^3/ft^3)]. For $L_c = 3$ mm, for example, the right graph in figure 17 shows that the measured inclusion volume fraction (for $d_{inc} \geq 1.5$ mm) is predicted for approximately $L_{agg} = 4$ mm. However, for $L_c = 3$ mm and $L_{agg} = 4$ mm, the left graph shows that the predicted inclusion number density is much larger than the measured one. If one chooses a smaller agglomeration length, say $L_{agg} \approx 1$ mm, the inclusion number density (for $d_{inc} \geq 1.5$ mm) can be predicted correctly, but the volume fraction (for $d_{inc} \geq 1.5$ mm) is generally too small. It is believed that this inability to find characteristic and agglomeration lengths that result in good agreement with the measurements is related to the fact that the present model is unable to predict sufficiently large inclusions in the plate portion of the casting, regardless of the value chosen for L_c and L_{agg}. Nonetheless, a reasonable compromise is achieved for $L_c = 4$ mm and $L_{agg} = 3$ mm; this combination is denoted with a red 'X' in figure 17. With those values for L_c and L_{agg},

the measured inclusion volume fraction in the plate is under-predicted by about 60% and the measured inclusion number density in the plate is over-predicted by about 170%. However, the predicted inclusion number density and volume fraction for the entire casting (see figure 15 for $d_{inc} \geq 1.5$ mm) are in somewhat better agreement with the measurements (i.e., the volume fraction is under-predicted by ~43% and the number density is over-predicted by ~102%). While these differences may seem to be overly large, the predictions are still well within one standard deviation of the measured inclusion volume fraction and number density averages for the 21 "dirty" plates (see figure 11). Furthermore, if the 17 "clean" plates were included in forming the averages, the above comparison would yield very different results. Clearly, progress can only be made if more accurate and repeatable experimental measurements become available. Nonetheless, the values for L_c and L_{agg} established above appear to be of a reasonable magnitude.

Additional simulations were conducted where the pour time and the head height of the liquid steel above the top of the pouring cup were varied. The results of this parametric study are shown in figure 18. In the experiments, the head height varies because the liquid steel level in the bottom-pour ladle is not constant. As indicated in figure 18, three combinations of (measured) pour times and head heights were simulated. Note that different head heights result not only in variations in the pour time, but also in the velocity of the metal stream entering the sprue. The left graph in figure 18 shows the predicted total inclusion volume fractions and the right graph shows the predicted integrated free surface areas [see equation (4)]. It is seen that the inclusion volume and the integrated free surface area are predicted to both increase with increasing pour time. This can be expected because a larger pour time causes the melt to be exposed to the atmosphere for a longer time. In fact, for identical conditions otherwise, the total inclusion volume formed can be expected to increase linearly with pour time [see also equation (5)]. However, a doubling of the pour time from 4 s to 8 s is predicted to produce an increase of only about 50% in the inclusion volume and the integrated free surface area. This can be explained by the fact that longer pour times (and lower head heights) result in lower melt velocities and a "smoother" free surface, with less area, during pouring. As already observed in figure 6, lower velocities result in lower mass transfer coefficients and, hence, smaller inclusion formation rates. With the present model, these factors are all taken into account simultaneously.

5. Conclusions and Recommendations

A model for simulating the formation and movement of reoxidation inclusions during pouring of carbon and low-alloy steel castings has been developed and implemented within MAGMAsoft. The model currently contains two adjustable parameters: the characteristic free surface length, L_c, and the agglomeration length, L_{agg}. Values for these two parameters have been established by comparing the model predictions to experimental measurements of total inclusion volume fraction and number density (with diameters above 1.5 mm) in cast steel weld plates. Overall, reasonably good agreement between the measured and predicted results has been achieved. Nonetheless, the present study points to the need for much additional research:

1. Additional plate casting experiments should be conducted in order to obtain more data on the inclusion volume fraction and number density in steel castings; the presence of risers above

the plate should be avoided since the inclusions inside of such risers cannot be measured; a large number of plates (e.g., > 50) should be cast under identical conditions in order to obtain statistically significant measurements; sets of experiments should be conducted where the pouring time or head height are systematically varied.

2. Since the inclusions in simple plates, such as the present weld plates, are distributed uniformly, the ability of the present model to predict final inclusion locations in a casting could not be tested; in particular, the observed tendency of inclusions to accumulate near the cope surface of steel castings[7] should be studied; measurements should be performed on complex shaped steel castings to obtain data on the inclusion distribution; such measurements should also help in developing a more realistic model for the interaction of an inclusion with the mold wall.

3. Models should be developed to calculate the characteristic free surface length and the agglomeration length as a function of the local flow and inclusion conditions (instead of assuming constant values, as in the present simulations). However, to develop and validate such models, much additional experimental work is needed as well.

4. It should be kept in mind that the inclusion predictions depend to a large extent on the quality of the filling simulation; current filling simulations do not necessarily resolve all details of the free surface geometry and dynamics during filling; grid independence studies should be conducted to verify that the inclusion predictions are not overly sensitive to the chosen grid; furthermore, the flow of the air and bubbles is not modeled at all; even if a full two-phase flow model is employed, it is unlikely that sufficient grid resolution can be achieved in a simulation of an entire casting to accurately compute phenomena such as local air entrainment at a free surface discontinuity, free-surface turbulence or breakup of liquid steel jets.

Acknowledgements

This work was supported by the Iowa Energy Center under grant number 06-01. It was also conducted under the auspices of the Steel Founders' Society of America, and through substantial in-kind support, guidance and interest from SFSA member foundries. The authors would like to thank Harrison Steel Castings Company and MAGMA GmbH for their generous support through donation of software, time and information.

References

[1] J.M. Svoboda, R.W. Monroe, C.E. Bates and J. Griffin (1987), "Appearance and Composition of Oxide Macroinclusions in Steel Castings," *AFS Transactions*, Vol. 95, pp. 187-202.

[2] J.A Griffin and C.E. Bates (1991), "Ladle Treating, Pouring and Gating for the Production of Clean Steel Castings," Steel Founders' Society of America Research Report No. 104.

[3] *MAGMASOFT*, MAGMA GmbH, Kackerstrasse 11, 52072 Aachen, Germany.

[4] L. Wang and C. Beckermann (2006), “Prediction of Reoxidation Inclusion Composition in Casting of Steel,” *Met. Mat. Trans. B*, vol. 37B, pp. 571-588.

[5] K.D. Carlson and C. Beckermann (2004), "Modeling of Reoxidation Inclusion Formation during Filling of Steel Castings,” in Proceedings of the 58th Technical and Operating Conference, SFSA, Chicago.

[6] W.E. Ranz and W.R. Marshall, Jr. (1952), “Evaporation from Drops,” *Chemical Engineering Progress*, vol. 48(4), pp. 141–146.

[7] M. Blair (2007), Private Communication, Steel Founders Society of America, Crystal Lake, IL.

[8] L. Zhang and B.G. Thomas (2003), “State of the Art in Evaluation and Control of Steel Cleanliness,” *ISIJ International*, vol. 43(3), pp. 271-291.

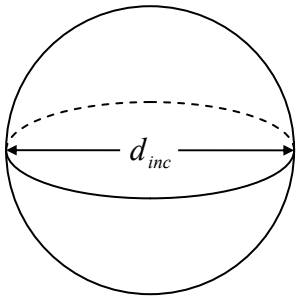

Figure 1. Spherical inclusion characterized by diameter, d_{inc}.

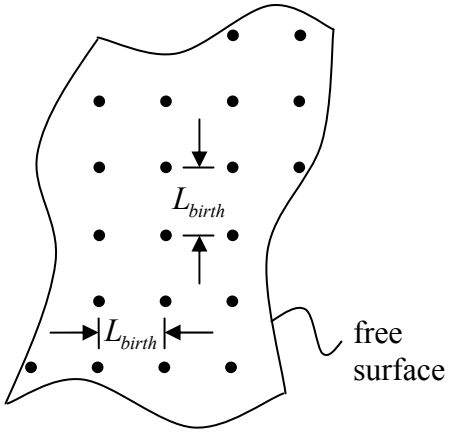

Figure 2. Schematic drawing of the spacing used in the birth model.

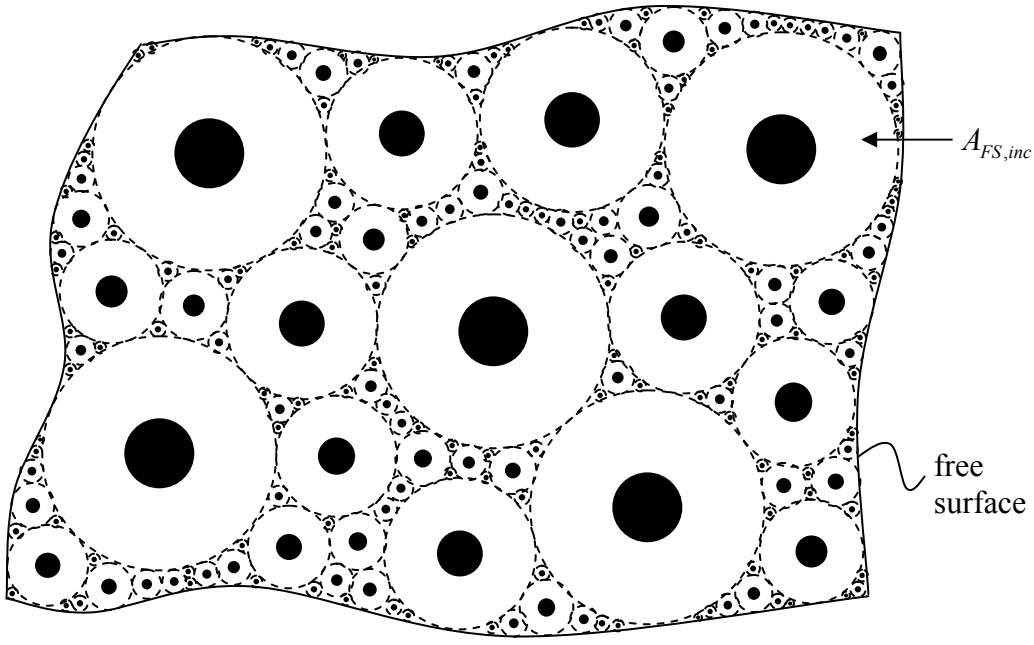

Figure 3. Schematic drawing of the inclusion surface areas used in the growth model.

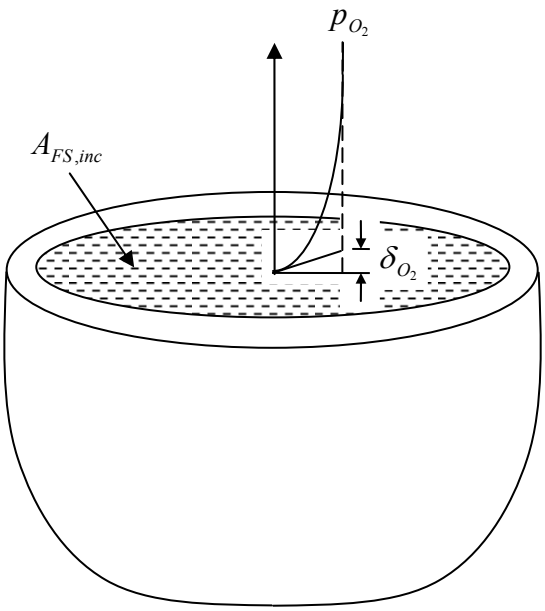

Figure 4. Illustration of the oxygen boundary layer above the melt free surface.

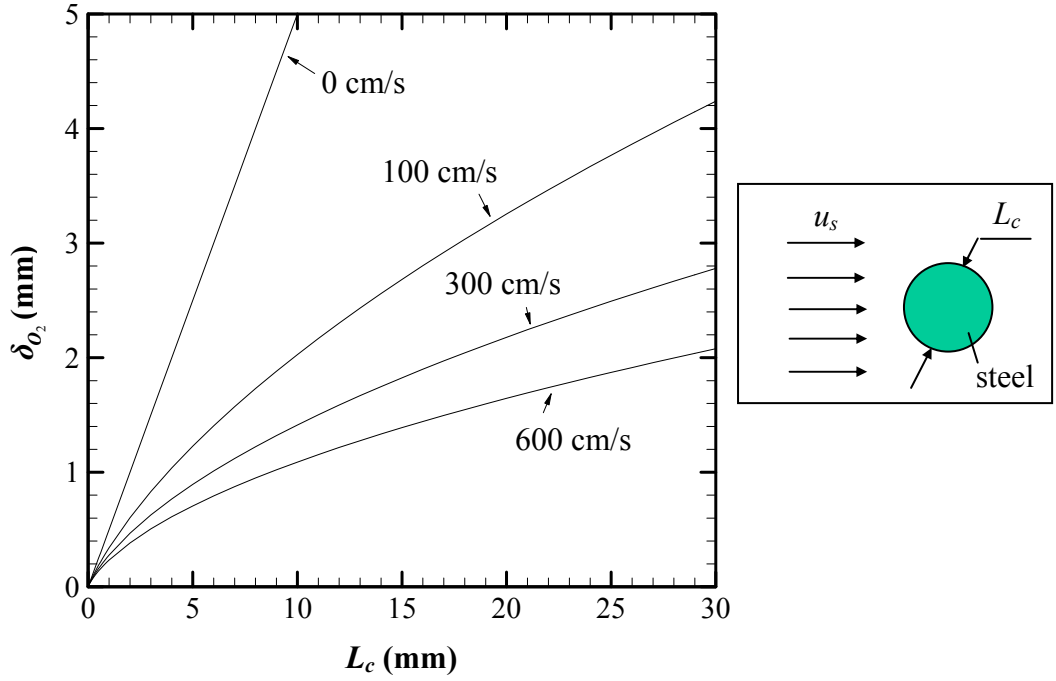

Figure 5. Predicted boundary layer thickness as a function of the characteristic free surface length, for several flow velocities.

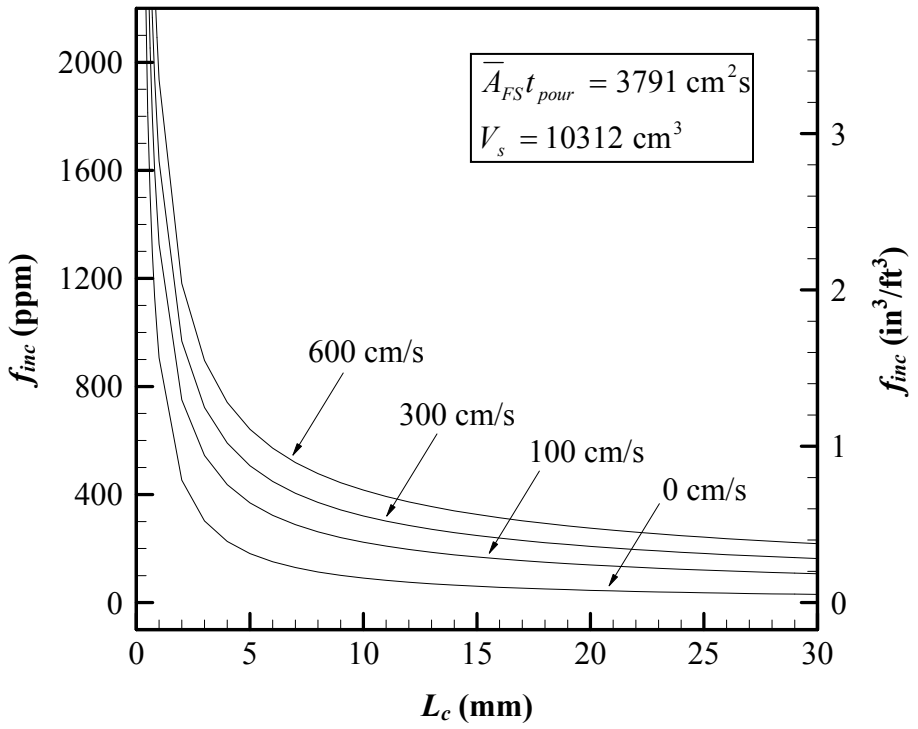

Figure 6. Predicted inclusion volume fraction as a function of the characteristic free surface length, for several flow velocities.

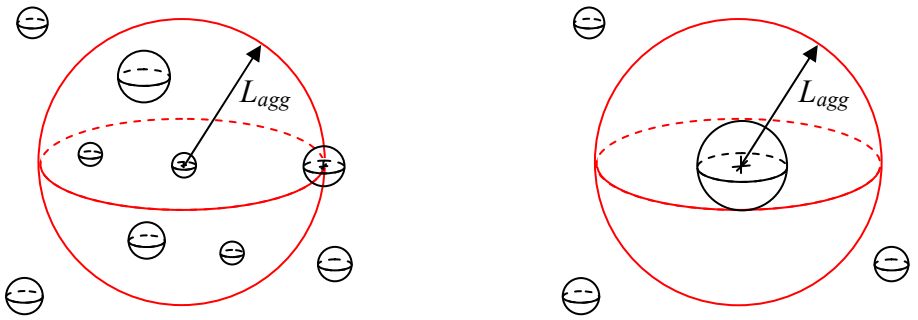

before agglomeration after agglomeration

Figure 7. Schematic demonstrating the agglomeration mechanism.

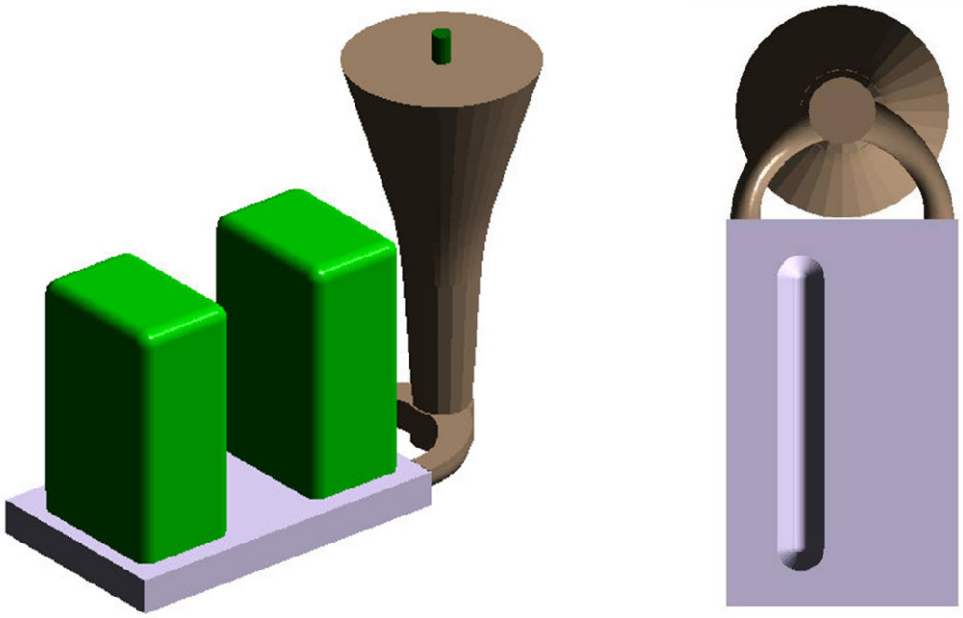

Figure 8. Two views of the weld plate steel casting used in the experiments.

Figure 9. Typical radiograph of a weld plate (with risers and gating removed), showing the presence of reoxidation inclusions.

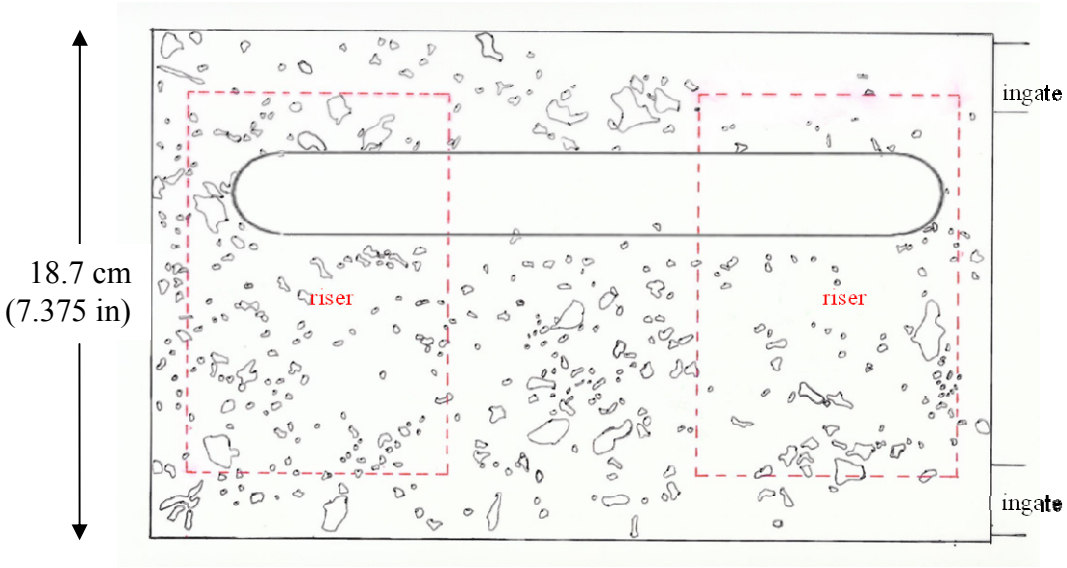

Figure 10. Superimposed traces of inclusions detected on the four "dirtiest" radiographs.

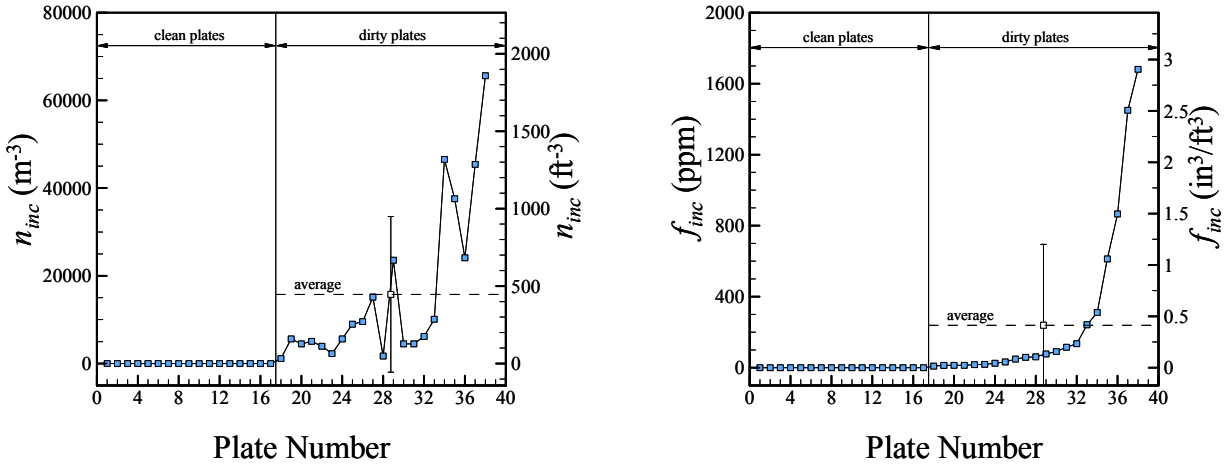

Figure 11. Measured inclusion number density (left graph) and volume fraction (right graph) for each of the 38 weld plates, ordered by increasing volume fraction; for the 21 "dirty" plates, the average inclusion number density and volume fraction are 15,756 m^{-3} (446 ft^{-3}) and 239 ppm (0.41 in^3/ft^3), respectively.

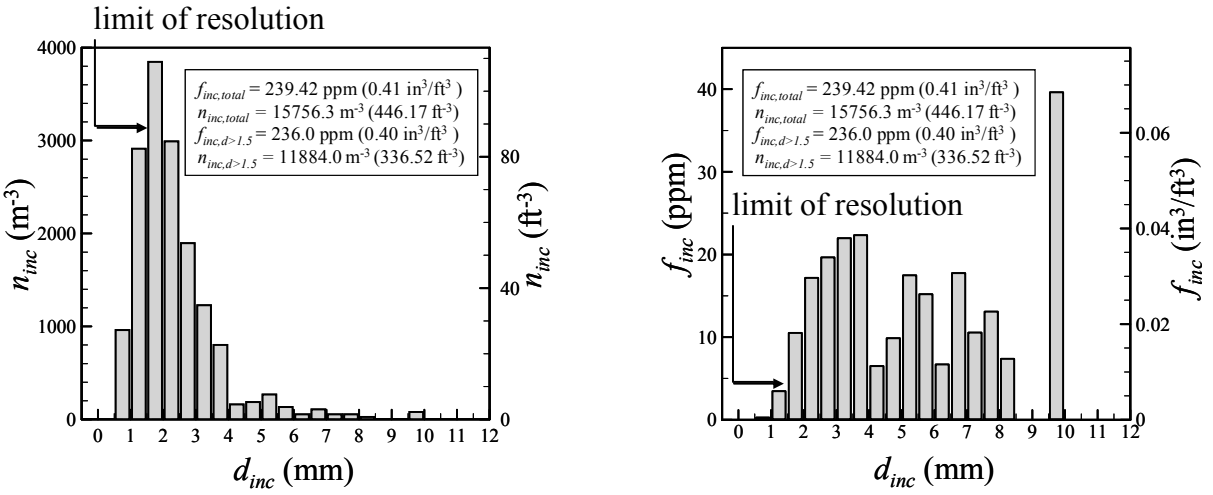

Figure 12. Measured inclusion number density (left graph) and volume fraction (right graph) distributions, in 0.5 mm wide diameter bins, for *all* 21 "dirty" weld plates; note that the limit of resolution is approximately 1.5 mm (~1/16 in); for inclusions larger than 1.5 mm in diameter, the average inclusion number density and volume fraction are 11,884 m^{-3} and 236 ppm, respectively.

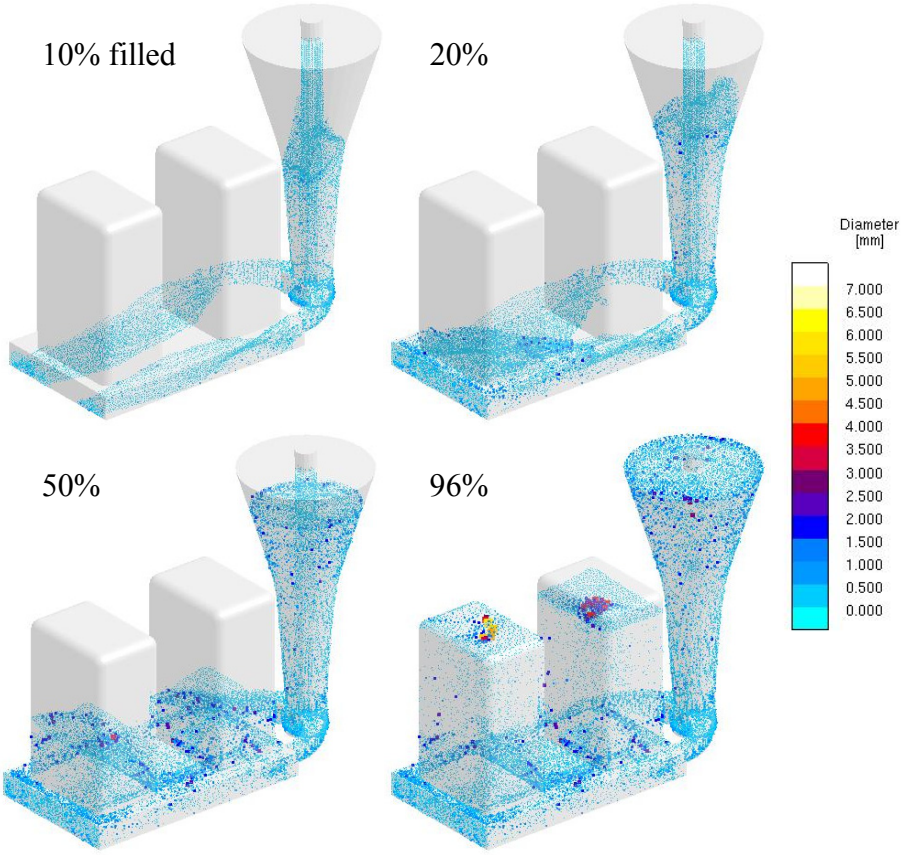

Figure 13. Predicted inclusions during filling ($L_c = 4$ mm, $L_{agg} = 3$ mm, inclusions stick when contacting mold wall).

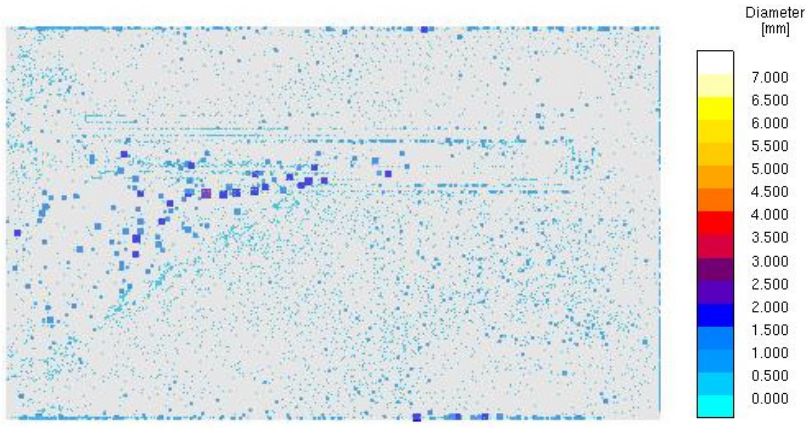

Figure 14. Predicted inclusions in the plate at the conclusion of filling ($L_c = 4$ mm, $L_{agg} = 3$ mm, inclusions stick when contacting mold wall).

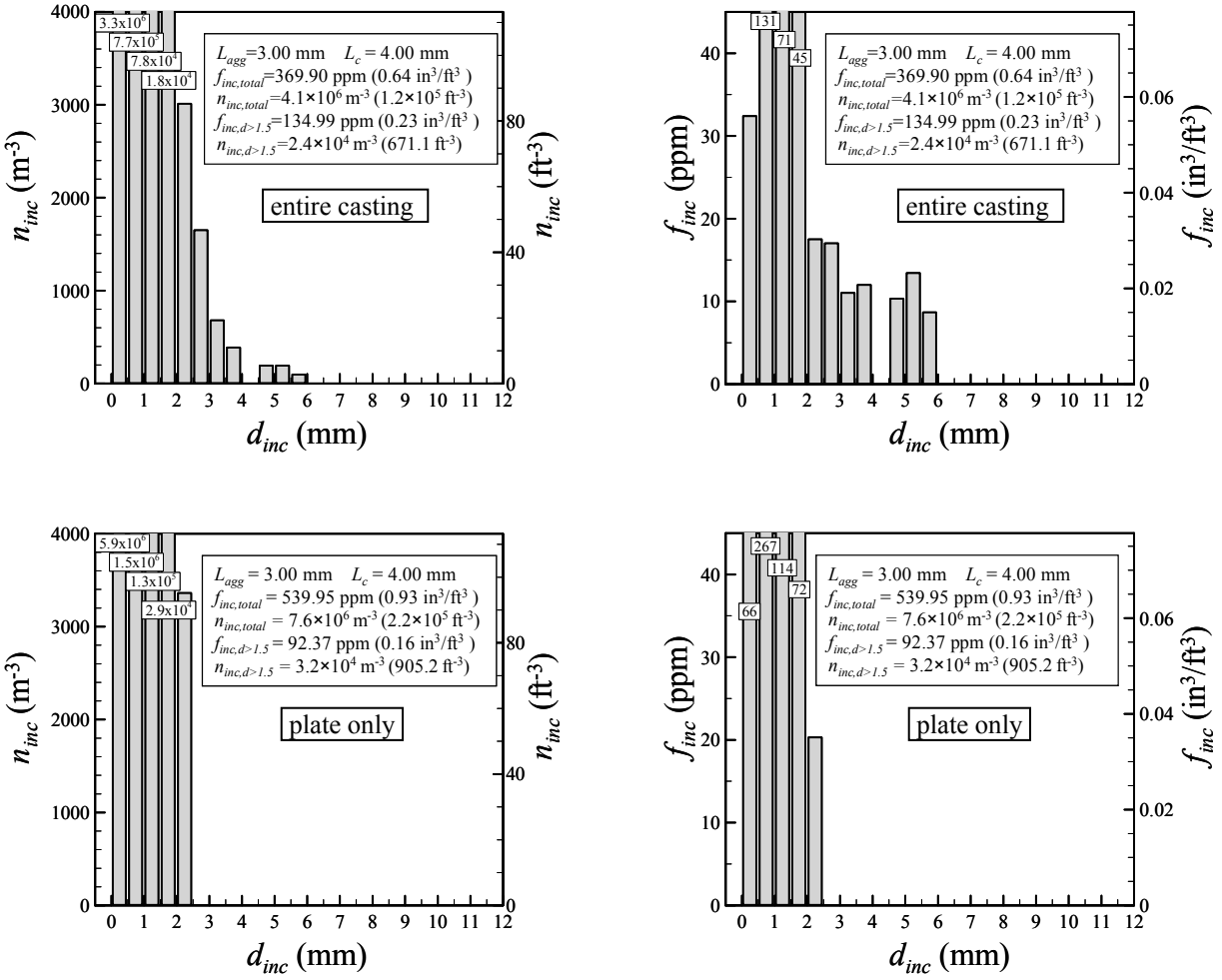

Figure 15. Predicted inclusion number density (left graphs) and volume fraction (right graphs); distributions for the entire casting (top graphs) and for the plate only (bottom graphs).

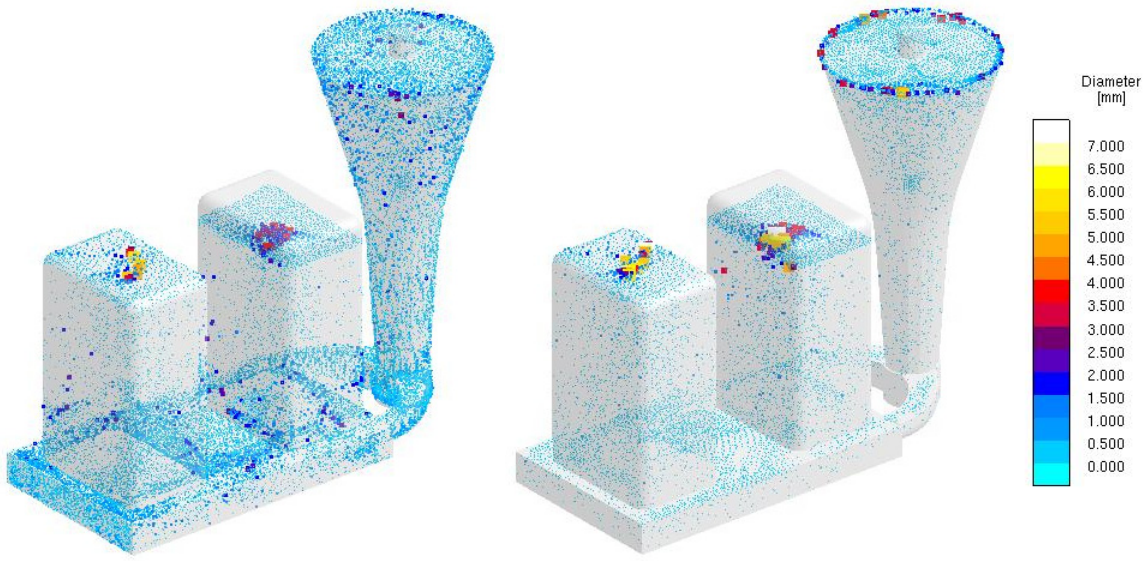

Figure 16. Comparison of simulation results obtained assuming that inclusions stick (left graph) and do not stick (right graph) to the mold walls ($L_c = 4$ mm, $L_{agg} = 3$ mm).

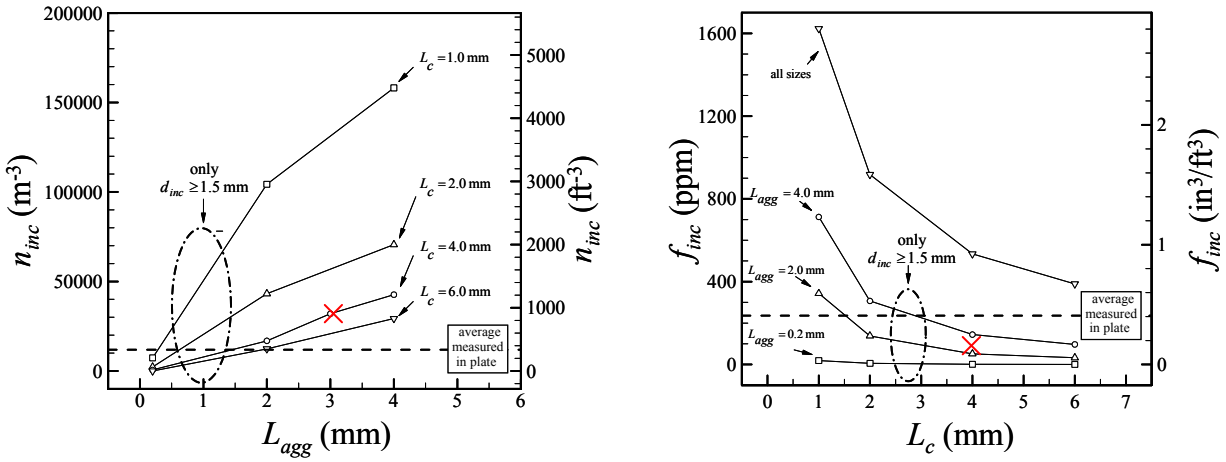

Figure 17. Predicted inclusion number density (left graph) and volume fraction (right graph) as a function of the characteristic free surface length, L_c, and the agglomeration length, L_{agg}; the results shown are for the plate only (not the entire casting); other than for the curve labeled "all sizes", the results are for inclusions with a diameter greater than 1.5 mm only.

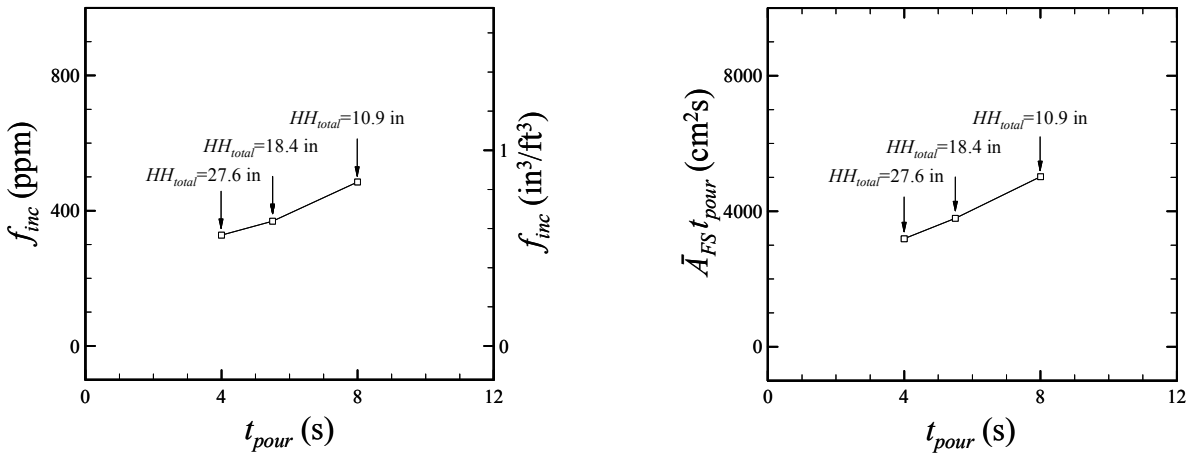

Figure 18. Predicted inclusion volume fraction (left graph) and integrated free surface area (right graph) as a function of the pour time of the casting; the total head height above the top of the pouring cup (HH_{total}) corresponding to each pour time is indicated in the graphs.